

Atmospheric stability effect on subgrid-scale physics for large-eddy simulation

Fernando Porté-Agel^{a,*}, Markus Pahlow^{b,d}, Charles Meneveau^{c,d}, Marc B. Parlange^{b,d}

^a Department of Civil Engineering, St. Anthony Falls Laboratory, University of Minnesota, Minneapolis, MN 55414, USA

^b Department of Geography and Environmental Engineering, The Johns Hopkins University, Baltimore, MD 21218, USA

^c Department of Mechanical Engineering, The Johns Hopkins University, Baltimore, MD 21218, USA

^d Center for Environmental and Applied Fluid Mechanics, The Johns Hopkins University, Baltimore, MD 21218, USA

Received 11 July 2000; received in revised form 5 February 2001; accepted 8 March 2001

Abstract

Field measurements in the atmospheric boundary layer were carried out to identify the effect of atmospheric stability on subgrid-scale physics for large-eddy simulation. The basic instrumentation setup consisted of 12 three-dimensional sonic anemometers arranged in two parallel horizontal arrays (seven sensors in the lower array and five sensors in the upper array). Data from this setup are used to compute the subgrid-scale (SGS) heat fluxes and SGS dissipation of the temperature variance under stable and unstable stability conditions. The relative contribution of the SGS vertical flux to the total turbulent flux increases when going from unstable to stable conditions. The relative importance of negative SGS dissipation (backscatter) events becomes larger under stable conditions. The model coefficients for two well-known SGS models (eddy-viscosity and non-linear) are computed. Model coefficients are found to depend strongly on stability. Under both stable and unstable conditions, large negative SGS dissipation is associated with the onset of ejection events while large positive SGS dissipation tends to occur during the onset of sweep events. These findings are also supported by conditionally sampled 2D velocity and temperature fields obtained using the 12 anemometers placed in a vertical array. © 2001 Elsevier Science Ltd. All rights reserved.

Keywords: Turbulence; Atmospheric boundary layer; Large-eddy simulation; Subgrid-scale modeling

1. Introduction

Large-eddy simulations (LESs) of the turbulent flow in the atmospheric boundary layer (ABL) provide multiscale, transient information necessary to better understand the dynamics of land–atmosphere exchange. Since it was first introduced [11], LES has been used to study the impact of different surface hydrologic factors such as the spatial variability of surface heat, moisture and roughness, on the ABL transport of momentum, heat and water vapor [1,2,18,20,25,46,55]. In LES, the unsteady 3D equations governing turbulent transport are numerically solved for scales of motion larger than a given grid size Δ , usually on the order of meters in simulations of the ABL. The contribution of the subgrid scales (smaller than Δ) on the resolved field is determined by a subgrid-scale (SGS) model. The separation

of scales between resolved and subgrid scales is achieved by using a filter, of characteristic width Δ , on the equations describing the transport of momentum and scalar quantities. This yields a set of equations for the evolution of the filtered (resolved) quantities, amenable to numerical solution on a grid with mesh size of order Δ .

In this paper we will focus on heat transport in the lower atmosphere. The equations for the conservation of filtered temperature $\tilde{\theta}$ are

$$\frac{\partial \tilde{\theta}}{\partial t} + \frac{\partial(\tilde{u}_j \tilde{\theta})}{\partial x_j} = -\frac{\partial q_i}{\partial x_i} + \tilde{Q}, \quad (1)$$

where t is time, x_j is the spatial coordinate in the j direction, u_j is the velocity component in the j direction, and \tilde{Q} is a source/sink term. Molecular dissipation has been neglected, and the tilde ($\tilde{\quad}$) denotes the filtering operation. The effect of the scales smaller than Δ on $\tilde{\theta}$ is through the SGS heat flux q_i (Eq. (1)), defined as

$$q_i = \tilde{u}_i \tilde{\theta} - \tilde{u}_i \tilde{\theta}. \quad (2)$$

* Corresponding author. Tel.: +1-612-627-4597; fax: +1-612-627-4609.

E-mail address: fporte@tc.umn.edu (F. Porté-Agel).

Note that q_i is unknown and must be parameterized with an SGS model as a function of the resolved velocity and temperature fields. The subgrid scales are known to have an important effect on the resolved scalar field [37]. For example, the dominant effect on the filtered scalar variance $\sigma_\theta^2 = \langle \frac{1}{2} \theta'^2 \rangle = \frac{1}{2} \langle (\bar{\theta} - \langle \bar{\theta} \rangle)^2 \rangle$, where $\langle \rangle$ denotes the ensemble average and the prime is defined by $\theta' = \bar{\theta} - \langle \bar{\theta} \rangle$, is through the so-called SGS dissipation rate of scalar variance

$$\chi = -q_j \frac{\partial \bar{\theta}'}{\partial x_j}. \quad (3)$$

Note that χ is also equal to the production of unresolved scalar fluctuations. Further details on the evolution equation for σ_θ^2 can be found in Porté-Agel et al. [45].

The relative contribution of the subgrid scales to the overall turbulent fluxes is very large near the land surface [46]. Hence, simulation results near the ground are particularly sensitive to the model formulation and this becomes especially important in a hydrologic context when one wishes to simulate latent and sensible heat flux into the atmosphere over natural land surfaces. Substantial effort is required to improve SGS parameterizations in order to make LES a reliable tool to simulate the physics of the near-ground land-atmosphere exchange. A key challenge for substantial progress in SGS modeling is to understand the relation between the dynamics and statistics of subgrid scales and the large scale dynamics of the flow [37]. The LES community has recognized the need to carry out so-called a priori studies that use experimental data to learn about the two-way relationship between subgrid and resolved scales that needs to be captured by the SGS models [42]. We present some of the latest developments in a priori studies, with particular emphasis on studies carried out in the lower atmosphere.

A priori studies use data at high spatial resolution. From these well resolved turbulent fields the SGS variables (fluxes and dissipation) can be computed and SGS models can be tested directly. The first a priori studies used data from direct numerical simulations (DNS) of isotropic turbulence [10,14] and other turbulent flows [19,42]. In contrast to LES, DNS resolves all the scales of motion (from the integral scale l to the Kolmogorov scale η) by using a grid size Δ smaller than η , therefore not requiring the use of an SGS model. For this reason, DNS results are often considered as ‘true’ experimental data. However, due to limitations in computational resources, DNS can only be used in relatively low Reynolds number flows ($Re \lesssim 10^4$). In order to extend a priori studies to higher Re flows, high-resolution laboratory measurements have been carried out and have been applied to test SGS models [5,29–31,34,36,38,41].

In the last few years the first a priori field studies have been initiated in the atmospheric surface layer

[45,47,48,60]. Some of the issues addressed by these experimental studies under unstable atmospheric stability include: (1) the statistical nature of the SGS variables and the relation between SGS variables and large-scale structures of the flow such as coherent structures; (2) evaluation of the performance of different SGS models; and (3) scale-dependence (filter-size dependence) of the measured and modeled SGS variables. A brief summary of the key findings from a priori studies in the atmospheric surface layer is presented below.

1.1. Statistics of the SGS variables

A particularly important feature of any SGS model is the ability to reproduce the correct relation between SGS variables and large-scale features of the flow such as coherent structures. In turbulent boundary-layer flows, coherent structures are associated with the sweep/ejection nature of the flow, and their presence in the atmospheric surface layer is easily identified through ramps in the measured temperature signal [15,16,22,23,50,53,54,58]. Such coherent motions are well known to be responsible for a very important fraction (75% and more) of the total turbulent fluxes [15], and therefore it is important that SGS models used in LES of the ABL capture the relationship between the coherent structures and the dynamics of the non-resolved scales.

In boundary-layer flows, some a priori studies that use conditional averaging techniques have addressed the importance of coherent structures on the SGS dissipation. Using data from filtered DNS of channel flow, Piomelli et al. [43] found that backscatter of resolved kinetic energy tends to occur during sweeps, while positive SGS dissipation is associated with ejection events. Lin [27] used results from LES with an eddy-viscosity model to study the near-grid-scale (corresponding to the smallest resolved scales) energy dissipation. He concluded that during ejections, both forward and backscatter occur, and the same is true during sweep events. Porté-Agel et al. [47,48] reexamined this issue using different conditional averaging techniques and found that strong negative SGS dissipation occurred during the onset of ejections (transition from sweeps to ejections associated with strong temperature gradients), while large positive SGS dissipation occurred during the onset of sweeps. Tong et al. [60] focused on the statistical nature of the SGS stresses ($\tau_{ij} = \widetilde{u_i u_j} - \tilde{u}_i \tilde{u}_j$) in the filtered momentum equation. By studying the joint probability density functions (pdfs) of the filtered vertical velocities and of the vertical SGS stresses, they found that the important interactions among resolved and SGS motions involved the resolved vertical velocity. The horizontal resolved motions had little effect upon the SGS velocities.

1.2. Evaluation of SGS models

Field data have been used to compute the SGS and resolved (filtered) variables, and these variables have then been used to test the performance of different SGS models. Here we present a brief description of the most popular SGS models and their performance as evaluated from previous a priori field studies. Extensive reviews of these models and other recent developments in SGS modeling can be found in [32,37,44].

Eddy-diffusion (eddy-viscosity) models are the most commonly used models in LES of ABL flows [56]. These models parameterize the SGS fluxes (SGS stresses) as proportional to the resolved scalar (and velocity) gradients. Specifically, the i -component of the SGS heat flux modeled with the eddy-diffusion model is of the form

$$q_i^{\text{ed}} = -Pr_T^{-1} C_S^2 \Delta^2 |\tilde{S}| \frac{\partial \tilde{\theta}}{\partial x_i}, \quad (4)$$

where $|\tilde{S}| = (2\tilde{S}_{ij}\tilde{S}_{ij})^{1/2}$ is the resolved strain rate magnitude, $\tilde{S}_{ij} = \frac{1}{2}(\frac{\partial \tilde{u}_i}{\partial x_j} + \frac{\partial \tilde{u}_j}{\partial x_i})$ is the resolved strain rate tensor, C_S is the so-called Smagorinsky coefficient and Pr_T is the sub-grid Prandtl number. When a cut-off filter is used in the inertial subrange of isotropic, homogeneous turbulence, C_S is known to have a value of about 0.17 [26]. Although eddy-viscosity models can yield the correct flow statistics (mean values, variances and turbulent spectra) [46], field studies show as low as 20% correlation between the measured and modeled SGS variables [45,47]. Moreover, eddy-viscosity models are unable to yield backscatter (transfer of energy or temperature variance from the subgrid to the resolved scales) which is measured in the field.

The so-called similarity model, and non-linear (gradient) model which take advantage of the scale similarity or invariance of the dynamics at different scales in the inertial range of turbulence, have generated considerable interest in recent years [6,61]. The non-linear or gradient model is of the form

$$q_i^{\text{nl}} = C_{\text{nl}} \Delta^2 \frac{\partial \tilde{u}_i}{\partial x_k} \frac{\partial \tilde{\theta}}{\partial x_k}, \quad (5)$$

where C_{nl} depends on the filter type. The repeated index k corresponds to the directions involved in the filtering operation (i.e. $k = 1, 2, 3$ for a 3D filter and $k = 1, 2$ if a 2D filter – in the streamwise and spanwise directions – is used). Using the similarity and non-linear models (instead of only eddy-viscosity) a better correlation between measured stresses/fluxes and modeled SGS stresses/fluxes has been found in a priori field studies [48]. These models are able to reproduce the backscatter of energy and scalar variance [4,29,48,51]. However, when used in simulations, the similarity model or the non-linear model alone do not dissipate enough energy and typically yield numerically unstable simulations. In

order to avoid this problem, [4] proposed a mixed model, obtained by adding a dissipative eddy-diffusion term. When using the non-linear model, the resulting mixed model is

$$q_i^{\text{mix}} = -[Pr_T^{-1} C_S^2]^* \Delta^2 |\tilde{S}| \frac{\partial \tilde{\theta}}{\partial x_i} + [C_{\text{nl}}]^* \Delta^2 \frac{\partial \tilde{u}_i}{\partial x_k} \frac{\partial \tilde{\theta}}{\partial x_k}, \quad (6)$$

where $[Pr_T^{-1} C_S^2]^*$ and $[C_{\text{nl}}]^*$ are the mixed model coefficients. The mixed model combines the strengths of both the similarity (or non-linear) model and the eddy-viscosity model. Although successfully applied in a number of engineering flows [3,51], to date the mixed model approach has not been used widely in simulations of the ABL. An exception is the work of Kosovic [24], who used a non-linear model in LES of the ABL with significant improvements in the predicted flow field as compared to the simple eddy-viscosity model.

1.3. Scale-dependence

By using different instrument setups, characterized by different separation between anemometers, Porté-Agel et al. [48] explored the influence of the filter width Δ on the mean and conditionally averaged SGS variables computed in an unstable atmospheric surface layer. They found that the mean SGS fluxes increase with increasing filter size. Although on average the SGS dissipation did not change substantially with change in the filter size, strong positive and negative SGS dissipation associated with large-scale structures of the flow were relatively more important for large Δ (at the same height z). Porté-Agel et al. [48] computed the model coefficients for the eddy-diffusion model, non-linear model and mixed model by forcing a match between the mean modeled and measured SGS dissipation. They found experimental evidence for the dependence of the model coefficients on the filter scale Δ . This dependence, stronger at smaller z/Δ , is in good agreement with the results obtained from simulations (under neutral stability conditions) using the dynamic eddy-viscosity model [46].

The above results from both an a priori study and simulations show that under near-neutral and unstable stability conditions the statistics of the SGS fluxes and dissipation and the values of the model coefficient depend on two important length scales: the distance to the ground z , and the filter scale Δ . The fact that scale-dependence is more important for very small z/Δ ($\Delta \gtrsim z$) is due to the fact that in that limit the filter scale is near the upper limit (or even outside) of the inertial subrange (corresponding to length scales on the order of z). In that limit, scale-invariance, based on inertial range arguments, breaks down.

In this paper, we use high-resolution field measurements to study the effect of atmospheric stability, especially stable stability, on the nature of the SGS

variables. Despite the improved understanding of the SGS dynamics under unstable and near-neutral conditions, provided by the recent a priori studies, very little is known about the effect of stable atmospheric stability on the SGS variables and corresponding implications for SGS modeling. In Section 3.1 we explore how atmospheric stability impacts the SGS fluxes and dissipation of temperature variance. In Section 3.2 we explore the effect of stable stability on the model coefficient for eddy-viscosity and non-linear models. Finally, in Section 3.3 the relationship between large-scale coherent structures of the flow and the magnitude of the SGS dissipation is measured using conditional averaging techniques.

2. Experiment

The field experiment was carried out over a flat field at the Campbell Tract research field of the University of California at Davis during the summer of 1999. The instruments were placed near the north-eastern corner of a uniform, bare soil, rectangular section field some 600 m (north–south) by 300 m (east–west). Since the prevailing winds were from the south-west, this location guaranteed a long homogeneous fetch in the upwind direction. The soil surface had furrows in the north–south direction, and the average furrow depth was 10 cm.

Twelve Campbell Scientific CSAT3 triaxial sonic anemometers (path length = 10 cm) were used to simultaneously measure the longitudinal (u_1), lateral (u_2) and vertical (u_3) wind velocity components as well as the air temperature (θ). The sampling frequency was 20 Hz. The supporting meteorological measurements included

net radiation, water vapor concentration, relative humidity and skin temperature.

The data analyzed and presented here were collected during six 25-min periods during which the sensors were arranged in two different setups. A double horizontal array of sensors was used during four periods (denoted as A, B, C, and D), while a single vertical array of anemometers was used during the two remaining periods (denoted as E and F). The dates and starting times for the six periods are given in Table 1, together with details of the arrangement of the sensors and the turbulence and meteorological conditions. A description of the two setups is given below.

2.1. Horizontal setup

Data from the horizontal arrays of sonics were obtained on the afternoon and evening of June 6. The sonic anemometers were laid out in two parallel horizontal arrays aligned roughly perpendicular to the prevailing wind (see Fig. 1). The lower array, at $z_1 = 3.41$ m, had seven anemometers and the upper array, $z_2 = 3.92$ m, had five anemometers. The distance between adjacent sensors in the same array is $d = 0.40$ m (see Table 1). Figs. 2(a)–(c) show a sketch of the relative position of the anemometers. The reference system is chosen so that $i = 1, 2, 3$ correspond to the streamwise, spanwise and vertical directions, respectively. Since the spanwise direction (perpendicular to the direction of the mean wind for each period) does not correspond exactly with the direction of alignment of the sensors, a shift is applied to the time series based on Taylor's hypothesis in order to produce simultaneous readings in the positions corresponding to the x axis (dotted line in Fig. 2(b)). Therefore, the

Table 1
Summary of meteorological and turbulence conditions during the six 25-min measurement periods considered in this study

Meteorological and turbulence conditions	Period A	Period B	Period C	Period D	Period E	Period F
Day	June 6	June 6	June 6	June 6	June 16	June 16
Starting time for the 30-min period (LST)	2109	2250	1830	1615	1855	2314
Distance between adjacent sensors (d) (m)	0.405	0.405	0.405	0.405	–	–
Angle β ($^\circ$)	+12.2	+3.92	–15.5	+34.0	–24.7	+16.6
Filter size Δ (m)	1.95	2.02	1.95	1.70	2.00	2.00
Mean horizontal wind speed ($\langle u_1 \rangle$) (m s^{-1})	2.33	2.77	6.14	6.25	3.34	1.34
Mean air temperature ($\langle \theta \rangle$) (K)	290.4	287.4	297.8	298.7	302.6	292.1
RMS horizontal velocity (σ_{u_1}) (m s^{-1})	0.44	0.46	0.99	1.17	0.57	0.36
RMS vertical velocity (σ_{u_3}) (m s^{-1})	0.12	0.19	0.42	0.51	0.33	0.08
RMS temperature (σ_θ) (K)	0.51	0.27	0.21	0.98	0.38	0.09
Friction velocity (u_*) (m s^{-1})	0.047	0.10	0.28	0.41	0.24	0.040
Streamwise heat flux ($\langle u_1' \theta' \rangle$) (K m s^{-1})	0.0924	0.0371	0.0762	–0.4722	–0.0954	+0.0168
Vertical heat flux ($\langle u_3' \theta' \rangle$) (K m s^{-1})	–0.0068	–0.0100	–0.0222	0.1530	+0.0520	–0.0010
Obukhov length (L) (m)	1.36	9.16	196.36	–31.71	–19.58	4.39
Stability parameter (z/L)	2.47	0.37	0.02	–0.11	–0.14	0.64
Surface temperature (K)	286.2	284.0	292.8	298.9	304.5	291.3

Periods A, B, C and D used data collected with two horizontal parallel arrays of anemometers, while periods E and F used data from a single vertical array.



Fig. 1. Photograph showing the double horizontal array of 3D sonic anemometers.

distance between two consecutive sensors in the x direction is $\Delta = d \cos \beta$, where β is the angle between the direction of the mean wind and the direction perpendicular to the sensors. The values of β and d corresponding to the four periods (A, B, C and D) are given in Table 1. From Table 1, the four periods show very distinct atmospheric stabilities. In particular, the values of the stability parameter z/L are +2.47 for

period A (stable), +0.37 for period B (moderately stable), +0.02 for period C (weakly stable), and -0.11 for period D (unstable). The Obukhov length L is defined as

$$L = \frac{-u_*^3 \rho}{kg \left[\frac{H}{c_p(\theta)} + 0.61E \right]}, \quad (7)$$

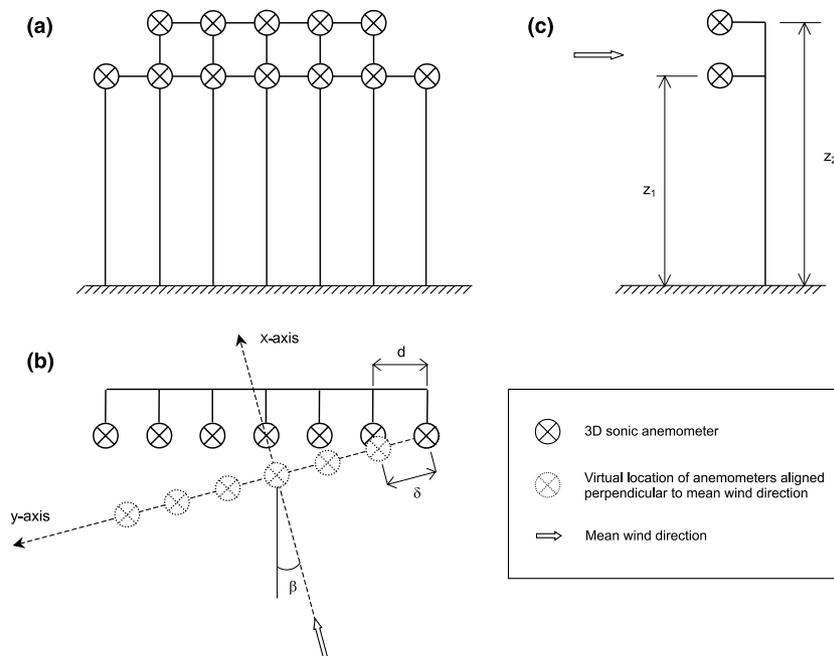


Fig. 2. Sketch of the instrument setup. (a) Front view; (b) top view; and (c) lateral view.

where $u_* (= [\tau/\rho]^{1/2} = [-\langle u'_1 u'_3 \rangle]^{1/2})$ is the friction velocity, τ is the surface shear stress, ρ is the density of air, H is the sensible heat flux, $\langle \theta \rangle$ is the mean air temperature, E is the water vapor flux ($E = \rho \langle u'_3 q' \rangle$), q' is the fluctuation in the water vapor concentration, g is the gravitational acceleration, and k ($=0.4$) is von Karman's constant. The soil was relatively moist due to an irrigation during the afternoon of June 5.

In Figs. 3 and 4, 2D color contour plots of the streamwise velocity (u_1) at the two heights (z_1 and z_2), as well as of the vertical velocity (u_3) and temperature (θ) at the lower level (z_1), are shown corresponding to the measurement periods D (unstable conditions) and A (stable conditions), respectively. The short axis corresponds to the direction perpendicular to the main wind (y direction). The longer axis corresponds to the direction of the main wind (x direction), and is obtained using Taylor's hypothesis to convert the time coordinate into a space coordinate.

In Figs. 3 and 4 the presence and size of structures of the flow can be observed. Note that the observed structures are smaller for stable conditions (Fig. 4) than for unstable conditions (Fig. 3). Under unstable con-

ditions (Fig. 3), ejections ($u'_3 > 0$) carry relatively warm air from the near-ground region upwards, producing an increase in the temperature ($\theta' > 0$), while under stable conditions (Fig. 4) ejections move relatively cool air upwards.

The power spectra for the streamwise velocity and temperature signals measured at height $z = z_1$ ($= 3.41$ m) are computed and presented in Figs. 5(a) and (b) corresponding to periods A (stable) and B (moderately stable), respectively. They are obtained from 25 segments of 1024 points each, using a Bartlett window [49]. In Fig. 5 the power spectra (E_k for a generic signal k) are normalized as $E_k/(\sigma_k^2 z)$, where σ_k^2 is the variance of the signal. The wave number k_1 is based on the sampling frequency, using Taylor's hypothesis, and it is normalized by z . The slope of the spectra is $-5/3$ for a considerable range of wave numbers, which corresponds with the inertial subrange. For period A, the spectral slope is much smaller (~ -1) at relatively small wave numbers ($k_1 z \lesssim 3$). Due to the damping effect of strong stratification, the characteristic scale of turbulence under stable conditions ($\sim L$) is smaller than it is under neutral conditions ($\sim z$). Hence, for stable condi-

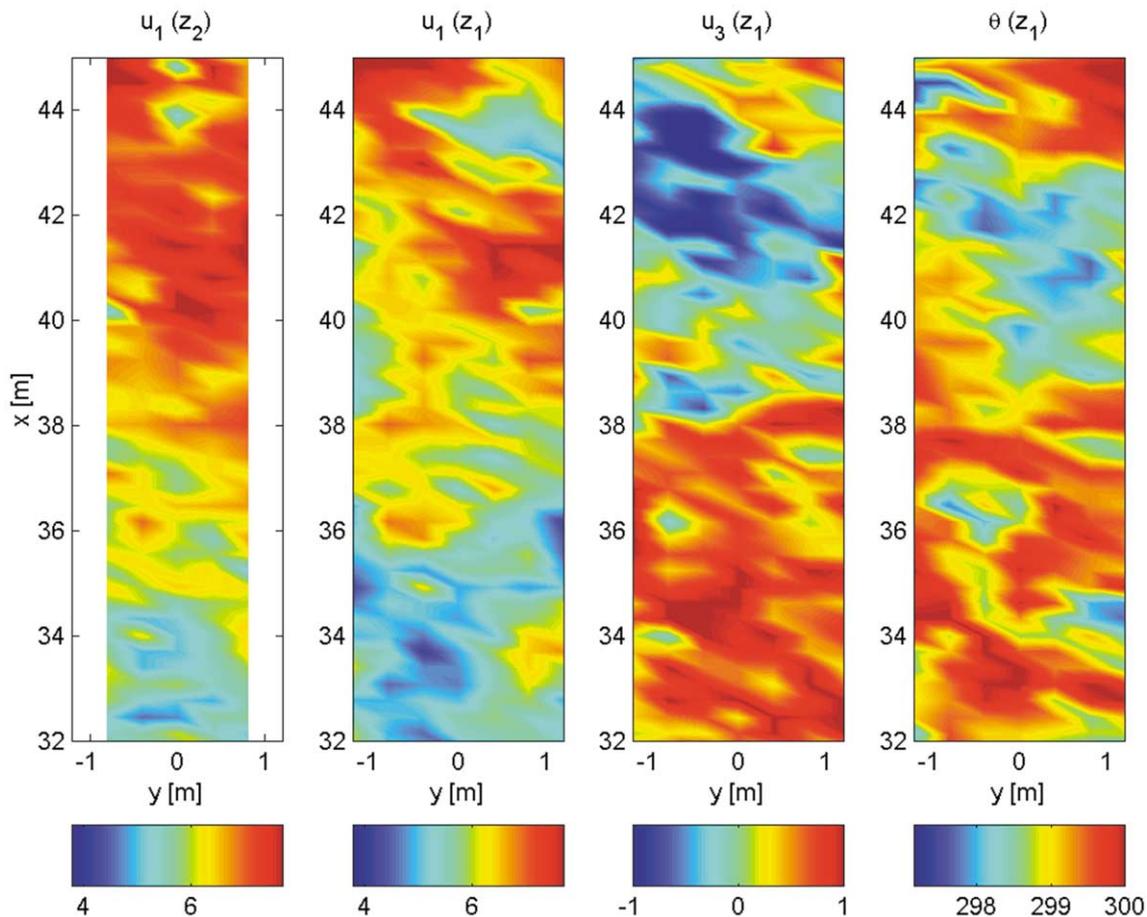


Fig. 3. Horizontal contour plots of the streamwise velocity (u_1 in m s^{-1}) at the two heights (z_1 and z_2), vertical velocity (u_3 in m s^{-1}) at $z = z_1$, and temperature (θ in K) also at $z = z_1$, corresponding to measurement period D (unstable).

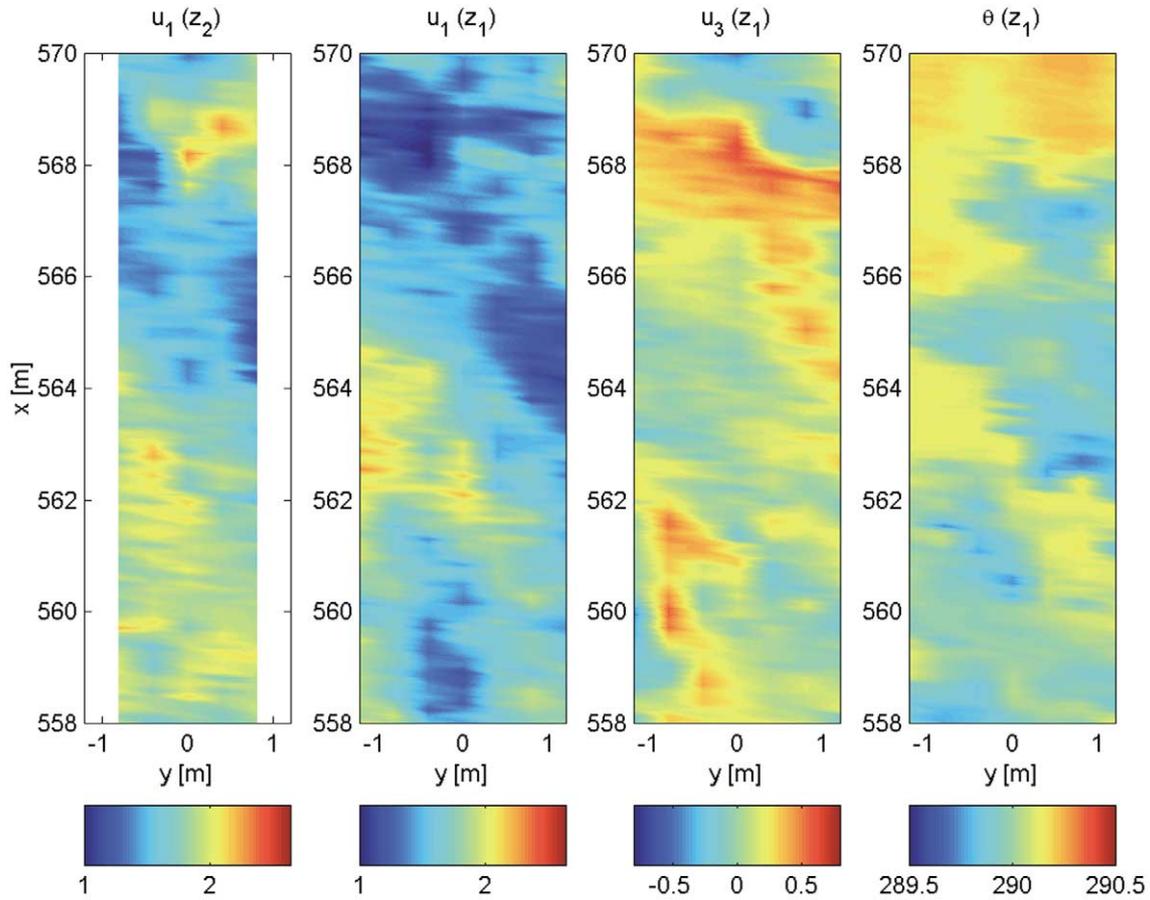


Fig. 4. Horizontal contour plots of the streamwise velocity (u_1 in m s^{-1}) at the two heights (z_1 and z_2), vertical velocity (u_3 in m s^{-1}) at $z = z_1$, and temperature (θ in K) also at $z = z_1$, corresponding to measurement period A (stable).

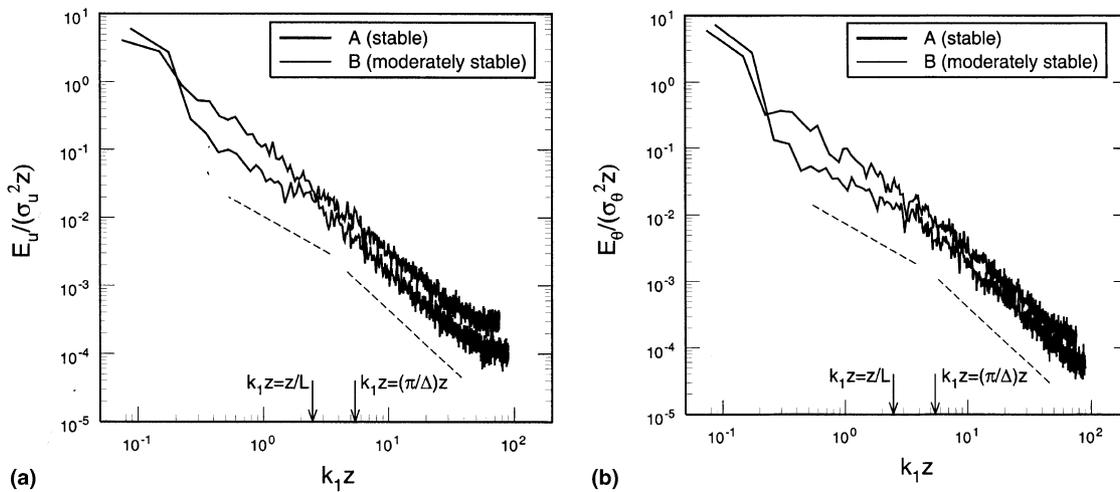


Fig. 5. Normalized power spectra for the streamwise velocity (a) and the temperature (b) for measurement periods A (stable) and B (moderately stable). The $-5/3$ and -1 power laws are also shown (dashed lines). The arrows show $k_1 z$ corresponding to z/L ($= 2.47$ for period A) and to the filter scale Δ (see Section 3.1).

tions the inertial subrange (and thus the $-5/3$ spectral slope) is expected to have an upper limit at scales on the order of L (i.e. $k_1 L \approx 1$, or $k_1 z \approx z/L = 2.5$). In Fig. 5, we indicate scales that are relevant to our analysis:

$k_1 z = z/L$, where the transition starts for the most stable case, and $k_1 z = (\pi/\Delta)z$, the filter scale. For the other three periods (B, C and D), corresponding to weaker stability (even unstable conditions for period D), the

characteristic scale of turbulence is larger ($\sim z$) and therefore the inertial subrange behavior extends to smaller wave numbers than $k_1 z = z/L$. Since spectra from periods B, C and D showed a similar behavior, for presentation purposes only periods A and B are shown in Fig. 5.

2.2. Vertical setup

The vertical setup (used during the periods E and F) consists of a vertical array with the 12 3D sonic anemometers placed at heights (measured from the bottom of the furrows) $z_{(1)} = 1.53$, $z_{(2)} = 1.79$, $z_{(3)} = 2.03$, $z_{(4)} = 2.29$, $z_{(5)} = 2.55$, $z_{(6)} = 2.80$, $z_{(7)} = 3.06$, $z_{(8)} = 3.31$, $z_{(9)} = 3.56$, $z_{(10)} = 3.82$, $z_{(11)} = 4.06$, and $z_{(12)} = 4.32$ m, respectively (see Fig. 6). Note that the parenthesis in the subscripts indicate that the heights correspond to the vertical setup (as opposed to the double horizontal array). From Table 1, measurement periods E and F are unstable ($z/L = -0.14$) and stable ($z/L = 0.64$), respectively. The soil on June 16 was dry compared to the conditions on June 6 (horizontal setup), since there was no further irrigation after June 5. Data collected during periods E and F are used in Section 3.3 to study the qualitative effect of a change in atmospheric stability on the vertical distribution of coherent structures of the flow during strong positive and negative dissipation events.



Fig. 6. Photograph showing the vertical array of 3D sonic anemometers.

3. Results

3.1. Statistics of the SGS heat flux and SGS dissipation

The SGS heat fluxes, q_i , and the SGS dissipation of temperature variance, χ , are computed using their definitions (Eqs. (2) and (3), respectively). A spatial filter of size Δ was applied to the measured velocities u_i , temperature θ , and products $u_i\theta$, to obtain the SGS fluxes ($q_i = u_i\theta - \tilde{u}_i\tilde{\theta}$). As in previous a priori studies [48,47], a 2D filter is used, consisting of a box filter in the spanwise direction (roughly parallel to the alignment of the sensors) and a Gaussian filter in the streamwise direction. Using results from simulations, Tong et al. [59] showed that in the atmospheric surface layer, 2D filtering obtained from arrays of sensors is a good approximation to 3D spatial filtering. In the spanwise direction, due to the limited number of points (equal to the number of sensors), a box filter is the most suitable choice. This was also shown by Cerutti and Meneveau [9] in the context of arrays of hot-wire sensors for similar studies in laboratory turbulence. In the streamwise direction, different filters were used (including box, cut-off, top-hat and Gaussian filters), with very similar results. For presentation purposes, in this paper we only show results obtained with a Gaussian filter. This filter represents a good trade-off in terms of filtering local effects with respect to the other filter types. The Gaussian filter yields smoother fields than the box filter that is more localized in space. Spectral cut-off filters on the other hand are not localized enough and when filtering spatially localized phenomena such as sharp gradients (e.g. those associated with the onset of ejection and sweep events), the spectral cut-off filter produces ‘ringing effects’ due to the Gibbs phenomenon with spatially non-local impact.

For a generic variable $\alpha(x, y, z)$, where x , y , and z are the streamwise (x_1), spanwise (x_2) and vertical (x_3) spatial coordinates, respectively, the filtered variable $\tilde{\alpha}(x, y_J, z_K)$, corresponding to the lateral position y_J and height z_K , is computed as follows: The box filter applied in the spanwise direction consists of the average $\bar{\alpha}(x, y_J, z_K) = \frac{1}{N} \sum_{j=1}^N \alpha(x, y_j, z_K)$, where y_j is the lateral position of each of the N sensors centered around the ordinate y_J . N was chosen to be 5 in order to maximize the number of sensors used to filter in the spanwise direction. This corresponds to a filter size $\Delta = 5 \times \Delta = 2.0$ m. The average $\bar{\alpha}(x, y_J, z_K)$ is then filtered in the streamwise direction by convolution with a filter function $G_\Delta : \tilde{\alpha}(x, y_J, z_K) = \int \bar{\alpha}(x, y_J, z_K) G_\Delta(x - x') dx'$, where x' is an integration variable. For computational convenience the filtering is done in wave space using the Fast Fourier Transform [49]. The results presented here were obtained using a Gaussian filter whose Fourier transform is of the form: $\hat{G}_\Delta = \exp(-(k_1^2 \Delta^2)/24)$, where k_1 is the wave number and Δ the filter size. The filter size was chosen to be $\Delta = 5 \times \Delta$, equal to the filter size in the

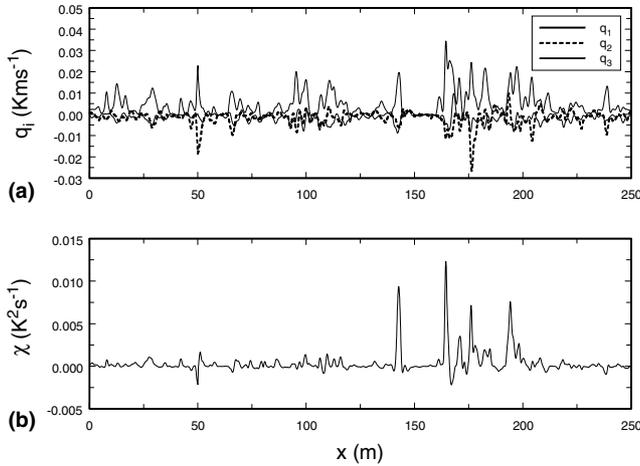


Fig. 7. (a) Portion of the three components of the SGS heat flux signals: streamwise q_1 (thick solid line), spanwise q_2 (dashed line) and vertical q_3 (thin solid line). (b) Portion of the SGS dissipation of the temperature variance χ (thick solid line). All signals correspond to measurement period A (stable).

transverse direction. As shown in Fig. 5, the selected filter size (wave number $k_1 = \pi/\Delta$) falls well within the inertial subrange, characterized by the $-5/3$ slope in the spectra.

To compute the SGS dissipation ($\chi = -q_j(\partial\tilde{\theta}'/\partial x_j)$), one needs to obtain the gradients of the filtered temperature fields. Streamwise derivatives are computed from time derivatives using Taylor’s hypothesis. The center difference approach is employed with the values of the filtered variables at positions $x = +\Delta/2$ and $x = -\Delta/2$ ($y_j = 0$). Vertical derivatives are computed using a one-sided finite difference approach with the values of the filtered variables at the vertical positions $z = z_2$ and $z = z_1$.

Fig. 7(a) shows a segment of the signals of the three components of the SGS heat flux q_i corresponding to the measurement period A (stable). The signals have a strong degree of intermittency, and q_1 and q_3 are anti-correlated. The magnitude of the mean values of the vertical flux $\langle q_3 \rangle$, presented in Table 2 for all the measurement periods, represent an important fraction

of the total fluxes $\langle u'_3\theta' \rangle$ presented in Table 1. From Tables 1 and 2, the relative contribution of $\langle q_3 \rangle$ to the overall flux $\langle u'_3\theta' \rangle$ increases with increasing stability (from 16% in the moderately unstable case to 47% under stable conditions). Figs. 8(a) and (b) are the probability density function (pdf) of q_1 and q_3 , respectively. The fluxes show a clear non-Gaussian behavior, with strong asymmetry in the pdfs of q_1 and q_3 . A clear change in the shape of the pdf is observed between the unstable period and the four stable cases. This is due to the different sign (and therefore direction) of the fluxes associated with a change in atmospheric stability (from unstable to stable). Under stable conditions, an incremental increase in stability is associated with a similar increase in the asymmetry of the pdfs of the fluxes.

Fig. 7(b) shows a segment of the SGS dissipation χ corresponding to the measurement period A (stable). The signal is highly intermittent and has negative values, indicative of backscatter (meaning the transfer of temperature variance from the subgrid scales to the resolved field). The mean value of the SGS dissipation $\langle \chi \rangle$, presented in Table 2 for all the measurement periods, decreases with increasing stability. This is consistent with the fact that the energy and temperature variance levels (and also the mean transfer from the resolved to the SGS) are damped with stable atmospheric stratification. The pdf of the measured SGS dissipation, shown in Fig. 9, is also very different from the Gaussian distribution. The marked asymmetry shows that the positive average value of $\langle \chi \rangle$ (forward cascade of scalar variance in the mean) is due to the fact that strong positive values occur more frequently, and are larger in magnitude, than negative values. The relative importance of backscatter events (negative SGS dissipation) increases with increasing stability. From the pdfs (not presented here) of all three ‘components’ of the SGS dissipation, we find that the third component, $-q_3(\partial\tilde{\theta}'/\partial x_3)$, is the one that contributes most to the trend in the negative tail of the pdf of the dissipation. Thus, the effect of strong stability on the subgrid scales is mainly through the vertical component of the SGS flux and SGS dissipation.

Table 2

Overall mean values and standard deviation (in brackets) of the measured SGS heat fluxes and SGS dissipation corresponding to measurement periods A (stable), B (moderately stable), C (weakly stable) and D (unstable)

SGS variable	Period A	Period B	Period C	Period D
Stability parameter (z/L)	2.47	0.37	0.02	-0.11
$\langle q_1 \rangle$ (K m s^{-1})	$+5.71 \times 10^{-3}$ (8.90×10^{-3})	$+5.36 \times 10^{-3}$ (11.84×10^{-3})	$+7.31 \times 10^{-3}$ (18.75×10^{-3})	-18.12×10^{-3} (63.58×10^{-3})
$\langle q_2 \rangle$ (K m s^{-1})	-0.99×10^{-3} (6.02×10^{-3})	-0.55×10^{-3} (7.42×10^{-3})	-1.82×10^{-3} (13.53×10^{-3})	$+4.24 \times 10^{-3}$ (55.12×10^{-3})
$\langle q_3 \rangle$ (K m s^{-1})	-3.20×10^{-3} (4.46×10^{-3})	-4.28×10^{-3} (6.39×10^{-3})	-7.58×10^{-3} (12.98×10^{-3})	$+24.21 \times 10^{-3}$ (54.63×10^{-3})
$\langle \chi \rangle$ ($\text{K}^2 \text{s}^{-1}$)	0.38×10^{-3} (1.90×10^{-3})	0.60×10^{-3} (2.13×10^{-3})	1.18×10^{-3} (3.82×10^{-3})	21.10×10^{-3} (79.5×10^{-3})

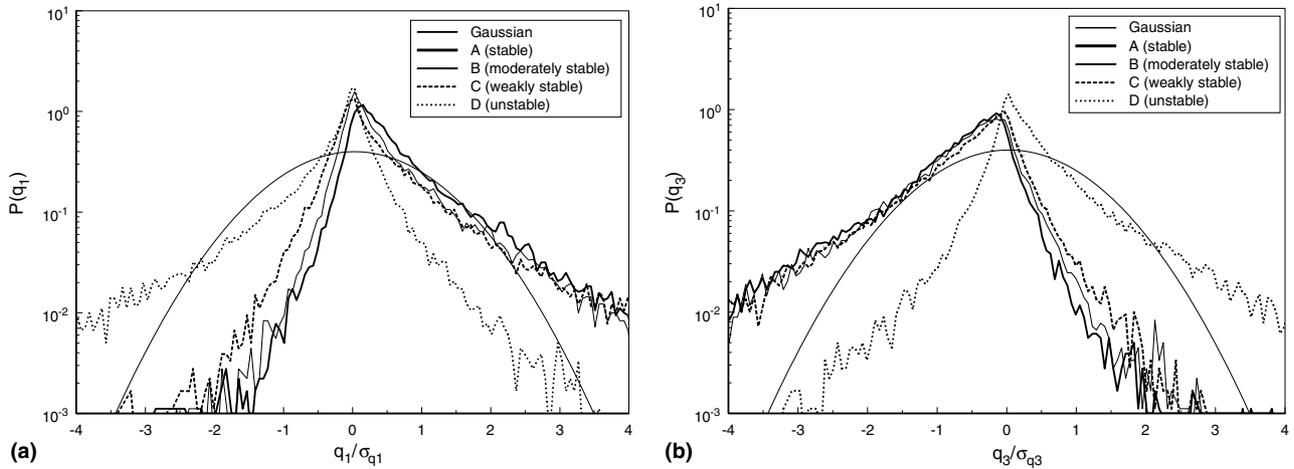


Fig. 8. Probability density function of the measured SGS heat flux components q_1 (a) and q_3 (b), normalized with their standard deviation, for measurement periods A (stable – thick solid line); B (moderately stable – thin solid line); C (weakly stable – dashed line); and D (unstable – dotted line). The fine solid line is the Gaussian distribution with zero mean.

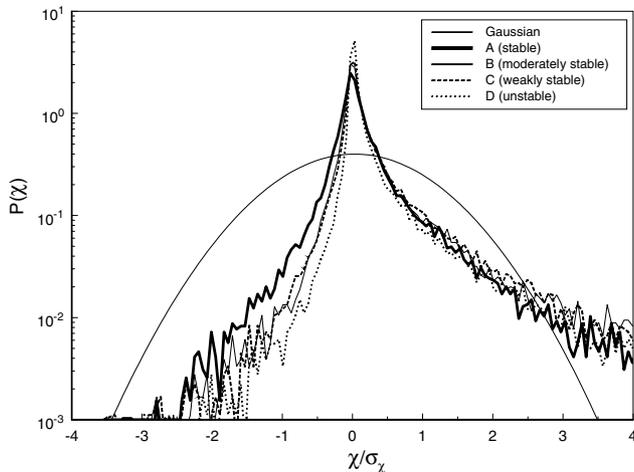


Fig. 9. Probability density function of the measured SGS dissipation of temperature variance χ for measurement periods A (stable – thick solid line); B (moderately stable – thin solid line); C (weakly stable – dashed line); and D (unstable – dotted line). The fine solid line is the Gaussian distribution with zero mean.

3.2. Effects of stability on model coefficients

We address the question of what effect, if any, increasing atmospheric stability has on the value of the SGS model coefficients. Efforts have been made to account for the effect of stable and unstable stratification on the model coefficients [7,8,13,21,52]. Most of the proposed formulations [8,13,52] account for stability corrections in the eddy-viscosity model by modifying the coefficient with an ad hoc function of the non-dimensional stability parameter. The trend in those models is that the coefficient decreases with increasing stability in order to take into account the reduction in the characteristic length scale (see e.g. Fig. 3 of [8]).

We consider the model coefficients of the eddy-diffusion model (Eq. (4)) and the non-linear model (Eq. (5)). Spatial derivatives of the filtered variables are needed for both models. They are computed in the same manner as the temperature gradients in Section 3.1. The model coefficients for the eddy-diffusion and non-linear models, $Pr_T^{-1}C_S^2$ and C_{nl} , respectively, are computed to guarantee that the mean modeled SGS dissipation matches the mean measured dissipation, i.e. $\langle \chi^{\text{mod}} \rangle = \langle \chi \rangle$ or $\langle -q_i^{\text{mod}} \frac{\partial \bar{\theta}'}{\partial x_i} \rangle = \langle -q_i \frac{\partial \bar{\theta}'}{\partial x_i} \rangle$. The coefficients obtained using this criterion are:

$$Pr_T^{-1}C_S^2 = \frac{\langle -q_i \frac{\partial \bar{\theta}'}{\partial x_i} \rangle}{\langle \Delta^2 |\bar{S}| \frac{\partial \bar{\theta}}{\partial x_i} \frac{\partial \bar{\theta}'}{\partial x_i} \rangle}, \quad (8)$$

and

$$C_{nl} = \frac{\langle q_i \frac{\partial \bar{\theta}'}{\partial x_i} \rangle}{\langle \Delta^2 \frac{\partial \bar{u}_i}{\partial x_k} \frac{\partial \bar{\theta}}{\partial x_k} \frac{\partial \bar{\theta}'}{\partial x_i} \rangle}. \quad (9)$$

In order to obtain an indication of the expected spread of the model coefficients for each measurement period the coefficients are computed for three subperiods of 8 min each. These values are used only as a qualitative measure of convergence.

Fig. 10 shows the mean value and the approximate standard deviation of the computed eddy-diffusion model coefficient $Pr_T^{-1}C_S^2$ as a function of the stability parameter z/L for the four periods (A, B, C and D) under consideration. Since the height of the instruments z is the same for all the periods, Fig. 10 shows a clear trend in the value of the model coefficient with changing stability (z/L). For the unstable case ($z/L = -0.11$) and weakly stable case ($z/L = +0.02$), $Pr_T^{-1}C_S^2 \sim 0.02$. This is in good agreement with previously reported values of $C_S \sim 0.09$ [12,42] and $Pr_T \sim 0.4$ [33,40]. In Fig. 10 a

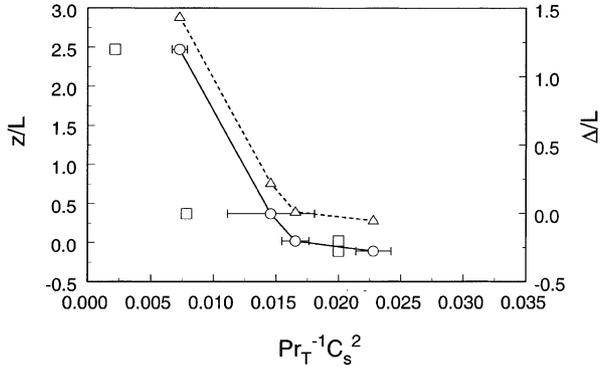


Fig. 10. Value of the eddy-diffusion model coefficient $Pr_T^{-1} C_S^2$ as a function of the stability parameter z/L (left axis) and Δ/L (right axis), obtained for the four measurement periods with different atmospheric stabilities. Period A: $L = 1.36$ m ($z/L = 2.47$); period B: $L = 9.16$ m ($z/L = 0.37$); period C: $L = 196.4$ m ($z/L = 0.02$); and period D: $L = -31.71$ m ($z/L = -0.11$). The open circles (left axis) and triangles (right axis) are obtained by matching the mean measured and modeled SGS dissipations. Squares (left axis) are obtained using Deardorff's correction. Results are averages over three values obtained using 8-min subperiods. The error bars for the open circles show the approximated standard deviation associated with those three samples.

change of atmospheric stability (from unstable to stable) is associated with a decrease in the value of $Pr_T^{-1} C_S^2$. And, for positive L , the value of the coefficient decreases with increasing atmospheric stability. Note that under the most stable conditions measured here, the value of $Pr_T^{-1} C_S^2$ is three times smaller than its value under moderately convective conditions. These results are in qualitative agreement with previously proposed empirical models [8,13]. In order to perform a quantitative comparison, we have computed $Pr_T^{-1} C_S^2$ by applying the stability correction proposed by Deardorff [13] to our measurements. This correction has been extensively used in LES of the ABL (e.g. [39,57]). In particular, Deardorff's original formulation corrects the length scale in an eddy-viscosity/diffusion model that uses the SGS turbulent kinetic energy e ($= \frac{1}{2} \overline{u_i u_i} - \frac{1}{2} \tilde{u}_i \tilde{u}_i$) to compute the SGS eddy-viscosity. As opposed to the model presented in Eq. (4), Deardorff's SGS model requires the explicit solution of a conservation equation for e . By applying Deardorff's length-scale correction to our eddy-diffusion model (Eq. (4)), $Pr_T^{-1} C_S^2$ can be computed as follows:

$$Pr_T^{-1} C_S^2 = (Pr_T^{-1} C_S^2)_o \quad \text{if } l_s \geq \Delta,$$

and

$$Pr_T^{-1} C_S^2 = (Pr_T^{-1} C_S^2)_o \left(\frac{l_s}{\Delta} \right)^2 \frac{1}{3} \left(1 + 2 \frac{l_s}{\Delta} \right) \quad \text{if } l_s < \Delta, \quad (10)$$

where $(Pr_T^{-1} C_S^2)_o \sim 0.02$ is the value of the coefficient for unstable and near-neutral conditions, and l_s is a mixing

length scale associated with stable stratification. l_s is defined as [13]

$$l_s = \frac{0.76 \langle e \rangle^{1/2}}{\left(\frac{g}{\langle \theta_o \rangle} \frac{\partial \langle \theta \rangle}{\partial z} \right)^{1/2}}, \quad (11)$$

where $\theta_o = \theta(1 + 0.61q)$ is the potential virtual temperature, and q is the specific humidity. $\langle \rangle$ denotes time averaging. The value of $Pr_T^{-1} C_S^2$ for each measurement period, obtained using Deardorff's stability correction (Eq. (10)), is presented in Fig. 10 (square symbols). The value of e is computed from the field data using its definition $e = \frac{1}{2} (\overline{u_i u_i} - \tilde{u}_i \tilde{u}_i)$. As compared to the results obtained from the measurements by balancing measured and modeled SGS dissipation, Deardorff's formulation yields substantially smaller coefficients associated with stable stratification. Canuto and Cheng proposed a different correction (see [8] for details) that yields results closer to our measurements, though still overestimating the effect of atmospheric stability.

The results presented in Fig. 10 can be related to previous findings by Porté-Agel et al. [48] in a similar field study, but using different filter sizes Δ and constant z and L , and simulation results using an eddy-viscosity scale-dependent dynamic model [46], that show a strong dependence of the eddy-viscosity and eddy-diffusion model coefficients on the ratio Δ/z when $z \lesssim \Delta$. They show that this scale-dependence becomes stronger for increasing Δ/z . In more general terms, scale-dependence of the model coefficient becomes important when the filter scale Δ approaches some characteristic large scale of turbulence l_t . For neutral stability, $l_t \sim z$. Under very strongly stable conditions, $l_t \sim L$. When cast as function of Δ/L (right axis of Fig. 10) one observes that the model coefficient changes most when $\Delta \sim L$ or larger (and $L > 0$). Thus, consistent with previous results, scale-dependence is stronger for larger values of Δ/l_t .

The values of the coefficient in the non-linear model, C_{nl} , obtained from the four periods are presented as a function of the stability parameter z/L and Δ/L in Fig. 11. Results also show scale-dependence associated with strong atmospheric stability. For the near-neutral and moderately stable/unstable cases, the coefficient has a value close to 0.3. This is consistent with the values reported in the literature [35]. For the stable case, C_{nl} is substantially larger (about twice as large). Again, this is further evidence for the relationship between scale-dependence and the relative importance of the characteristic turbulence length scale l_t with respect to the filter size Δ .

3.3. Conditional averaging and coherent structures

In this section we use two different conditional averaging techniques to study the relationship between coherent structures in the flow and the occurrence of

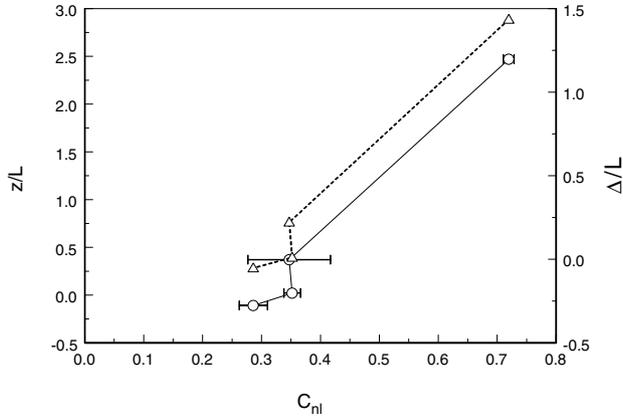


Fig. 11. Value of the model coefficient C_{nl} in the non-linear model, as a function of the stability parameter z/L (left axis) and Δ/L (right axis), obtained for the four measurement periods with different atmospheric stabilities. Period A: $L = 1.36$ m ($z/L = 2.47$); period B: $L = 9.16$ m ($z/L = 0.37$); period C: $L = 196.4$ m ($z/L = 0.02$); and period D: $L = -31.71$ m ($z/L = -0.11$). The open circles and triangles are obtained by averaging over three values obtained using 8-min subperiods. The error bars for the open circles show the approximated standard deviation associated with those three samples.

strong (positive or negative) SGS dissipation. Previous a priori field studies [45,47,48] using data collected under near-neutral and convective conditions indicate a high correlation between strong forward/backward scatter and strong negative/positive temperature gradients associated with the onset of sweeps/ejections in the flow. Here, the focus is on the effect of atmospheric stability on those results.

3.3.1. Conditionally averaged SGS dissipation based on temperature gradients

First, we perform conditional averaging on the SGS dissipation of the temperature variance based on the gradients in the resolved temperature field ($\partial\tilde{\theta}/\partial t$). This method takes advantage of the fact that under stable or unstable stratification coherent structures leave strong signatures in the form of ramp structures in the temperature field (see Section 1.2). For example, under stable conditions, ejections are associated with relatively low temperature values (since they transport cool air from the ground upwards) while sweeps are associated with relatively warm temperatures. As in [47], the conditional average of χ under some condition β in a window of size X is defined according to

$$\langle \chi | \beta \rangle(x') = \frac{1}{n} \sum_{i=1}^n \chi(x_i + x', y_j, z_k),$$

$$-\frac{X}{2} \leq x' \leq +\frac{X}{2}, \quad (12)$$

where x_i (with $1 \leq i \leq n$) are the points where χ satisfies the condition β . The conditional averages are computed

at $y_j = 0$ and $z_k = z_1$. For a point located at position $x' (= -t'U)$ in the averaging window, the conditional average $\langle \chi | \beta \rangle$ is computed by averaging all χ values at points that are located at a distance x' from the points that satisfy the condition (upstream if $x' < 0$ and downstream if $x' > 0$). For instance, for $x' = 0$ the value of the conditional average is computed from the values of χ at points that satisfy the condition.

In the first attempt to isolate different parts of ramp structures in the temperature field and relate them to the SGS variables, we use the two conditions used before by Porté-Agel et al. [47], based on the gradient of the resolved temperature signal.

Condition $\beta = \text{I}$: $\frac{\partial\tilde{\theta}}{\partial t} < -\sigma_{\partial\tilde{\theta}/\partial t}$, where $\sigma_{\partial\tilde{\theta}/\partial t}$ is the root mean square of $\partial\tilde{\theta}/\partial t$. This condition corresponds to a temperature drop in the time series. Under stable conditions, a relatively strong temperature drop tends to be associated with the onset of an ejection (the end of a sweep and the beginning of an ejection). Under unstable conditions, due to a change in the sign of the temperature gradients, condition I highlights the onset of sweep events.

Condition $\beta = \text{II}$: $\frac{\partial\tilde{\theta}}{\partial t} > \sigma_{\partial\tilde{\theta}/\partial t}$ corresponds to a temperature increase in the time series. This condition highlights the rising part of the temperature signal, which is typically associated with the onset of a sweep event under stable conditions.

The selection of the conditioning threshold, $\sigma_{\partial\tilde{\theta}/\partial t}$, is arbitrary and is selected simply to guarantee that it is large enough to isolate the local effects, and small enough to ensure the convergence of conditional averages. The width of the averaging window, X , was set to 20 times the filter width, i.e. $X = 40$ m. As in [45,47] the value of X has no effect on the average, but it allows us to show the entire portion of interest around $x' = 0$. The conditional average then asymptotes to the overall average as we move away from the center of the averaging window (at $x' = 0$). The number of points satisfying each condition was high enough to guarantee a good convergence of the conditional averages.

Fig. 12 shows the conditionally averaged SGS dissipation under condition I $\frac{\partial\tilde{\theta}}{\partial t} < -\sigma_{\partial\tilde{\theta}/\partial t}$, $\langle \chi | \text{I} \rangle$, for the four periods under consideration. Since the mean SGS dissipation is different for the four periods (see Section 3.1 and Table 2), the conditional averages are non-dimensionalized by the mean SGS dissipation $\langle \chi \rangle$. Under stable conditions, relatively strong drops in the temperature, associated with the onset of ejections, show a very small (even negative) SGS dissipation. The relative contribution of backscatter (negative SGS dissipation) becomes more important with increasing stability. This results in smaller (even negative under stable conditions) conditionally averaged dissipation. The increasing relative importance of backscatter with increasing stability is in good agreement with the shape of the pdf of χ presented in Fig. 9 for the different periods. Under un-

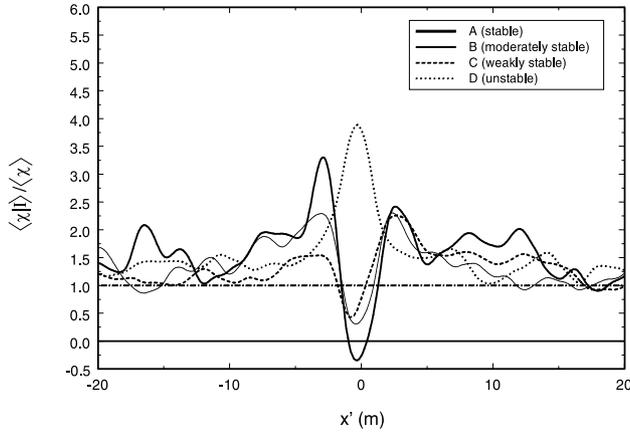


Fig. 12. Conditionally averaged SGS dissipation of temperature variance, under condition I ($\beta \equiv (\partial\theta/\partial t) < -\sigma_{\partial\theta/\partial t}$) for measurement periods A (stable); B (moderately stable); C (weakly stable); and D (unstable). The conditional averages have been normalized with the overall mean SGS dissipation $\langle \chi \rangle$.

stable conditions, temperature drops highlight the onset of sweeps (instead of the onset of ejections) and they are associated with very large (four times larger than average) SGS dissipation. These results are consistent with the results found by Porté-Agel et al. [47], also under convective conditions.

The conditionally averaged SGS dissipation under condition II ($\beta \equiv (\partial\theta/\partial t) > \sigma_{\partial\theta/\partial t}$, $\langle \chi | II \rangle$), is presented in Fig. 13. Under stable conditions, relatively strong increments in the temperature, associated with the onset of sweeps, show a very large positive SGS dissipation. In this case, temperature drops highlight the onset of ejections (instead of the onset of sweeps) and they are associated with relatively small SGS dissipations. Again, the relative importance of strong SGS dissipation (forward

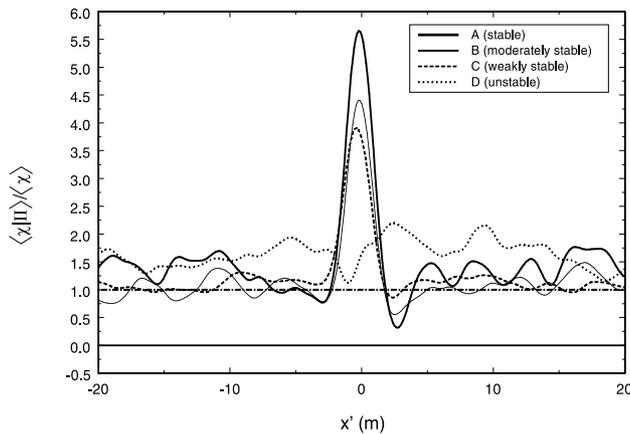


Fig. 13. Conditionally averaged SGS dissipation of temperature variance, under condition II ($\beta \equiv (\partial\theta/\partial t) > \sigma_{\partial\theta/\partial t}$) for measurement periods A (stable); B (moderately stable); C (weakly stable); and D (unstable). The conditional averages have been normalized with the overall mean SGS dissipation $\langle \chi \rangle$.

scatter in this case) events, and thus the value of the conditional average, appears to increase with increasing stability.

3.3.2. Conditionally averaged 2D velocity and temperature fields based on the SGS dissipation

We now use data from the vertical array of anemometers to isolate the structures of the flow responsible for strong positive (forward scatter) and negative (backscatter) SGS dissipation. In order to assess the qualitative differences associated with a change in stability, two periods are studied (periods E and F), corresponding to moderately unstable and stable atmospheric stability (see Table 1 for details on turbulence and meteorological conditions). For both periods, 2D (streamwise and vertical) wind velocity and temperature fields are conditionally averaged based on the value of the SGS dissipation. This approach was first used by Piomelli et al. [43] with DNS data of channel flow at low Reynolds numbers. Recently, Lin [27,28] used it to analyze LES results and Porté-Agel et al. [48] applied it to field data collected in the atmospheric surface layer under moderately unstable conditions.

Due to the lack of information in the spanwise direction, now the filtered variables (\tilde{u}_1 , \tilde{u}_3 or $\tilde{\theta}$) are obtained using a 1D filter (instead of a 2D filter). It consists of a Gaussian filter in the streamwise direction combined with Taylor's hypothesis in the same fashion as presented by Porté-Agel et al. [45,47]. For consistency with previous analysis, the filter size was chosen to be $\Delta = 2.0$ m. The SGS heat flux and a 2D surrogate of the SGS dissipation are computed at the height of the sixth sensor $z = z_{(6)} = 2.80$ m. Since derivatives cannot be computed in the spanwise direction, a 2D surrogate of the SGS dissipation is computed using the streamwise and vertical components, i.e. $\chi^{2D} = -q_1 \frac{\partial \theta'}{\partial x_1} - q_3 \frac{\partial \theta'}{\partial x_3}$. Note that the resolved (filtered) and SGS variables obtained using a 1D filter and a 2D surrogate of the SGS dissipation are expected to be quantitatively different from the ones obtained with a 2D or 3D filter and all three (including spanwise) components of the SGS dissipation χ . However, no significant changes in qualitative behavior are expected in terms of the conditional averages presented in this section. A comparison between conditionally averaged 1D and 2D filtered variables, showing their similar qualitative behavior, can be found in Porté-Agel et al. [47]. It was found that the effect of coherent structures on the SGS dissipation is mainly through the streamwise and vertical components, while the spanwise component is practically unaffected.

In this case the conditional average of the generic variable Φ ($\Phi = \tilde{u}_1$, \tilde{u}_3 or $\tilde{\theta}$) under condition β on a rectangular window of width X and height Z ($= z_{(12)} - z_{(1)}$) is defined as

$$\langle \Phi | \beta \rangle (x', z) = \frac{1}{n} \sum_{i=1}^n \Phi(x_i + x', z),$$

$$-\frac{X}{2} \leq x' \leq +\frac{X}{2} \quad \text{and} \quad z_{(1)} \leq z \leq z_{(12)}, \quad (13)$$

where x_i (with $1 \leq i \leq n$) is the streamwise coordinate of the points where Φ satisfies the condition β . Two conditions are used based on the value of the 2D surrogate of the SGS dissipation (χ^{2D}) obtained at $z = z_{(6)} = 2.80$ m.

Condition $\beta_{\chi^{2D}(+)}$: $\chi^{2D} > 3 \langle \chi^{2D} \rangle$, where $\langle \chi^{2D} \rangle$ is the overall average of the 2D surrogate of the SGS dissipation. This condition corresponds to large positive values of the SGS dissipation (strong forward scatter).

Condition $\beta_{\chi^{2D}(-)}$: $\chi^{2D} < -\langle \chi^{2D} \rangle$. This condition corresponds to relatively large negative values of the SGS dissipation, associated with backscatter of temperature variance.

The thresholds $3 \langle \chi^{2D} \rangle$ and $-\langle \chi^{2D} \rangle$ are again selected to guarantee good convergence of the conditional averaged fields. Note that the conditional average defined in Eq. (13) yields a 2D field for $\langle \Phi | \beta \rangle$. For a point of

coordinates (x', z) in the averaging window, the conditional average $\langle \Phi | \beta \rangle$ is obtained by averaging the value of Φ at all the points located at height z and at a distance x' (upstream for $x' < 0$ and downstream for $x' > 0$) from the point that satisfies the condition. In particular, points that satisfy the condition correspond to the coordinates $x' = 0$ and $z = z_{(6)} = 2.80$ m in the averaging window. From here on, this point is called the ‘reference point’.

The conditionally averaged wind velocity and temperature fields obtained during period E (unstable) using conditions $\beta_{\chi^{2D}(+)}$ and $\beta_{\chi^{2D}(-)}$ are presented in Figs. 14(a) and (b), respectively. From Fig. 14(a), large positive SGS dissipation (forward scatter) at the reference point, is associated with the transition between ejection events (downstream, i.e. $x' > 0$), bringing warm air upwards, and sweep events (upstream, i.e. $x' < 0$), carrying relatively cool air from aloft. This corresponds to a strong temperature increase in time at the reference point which is in good agreement with the results obtained for the unstable period D using conditional averaging based on temperature gradients. Strong

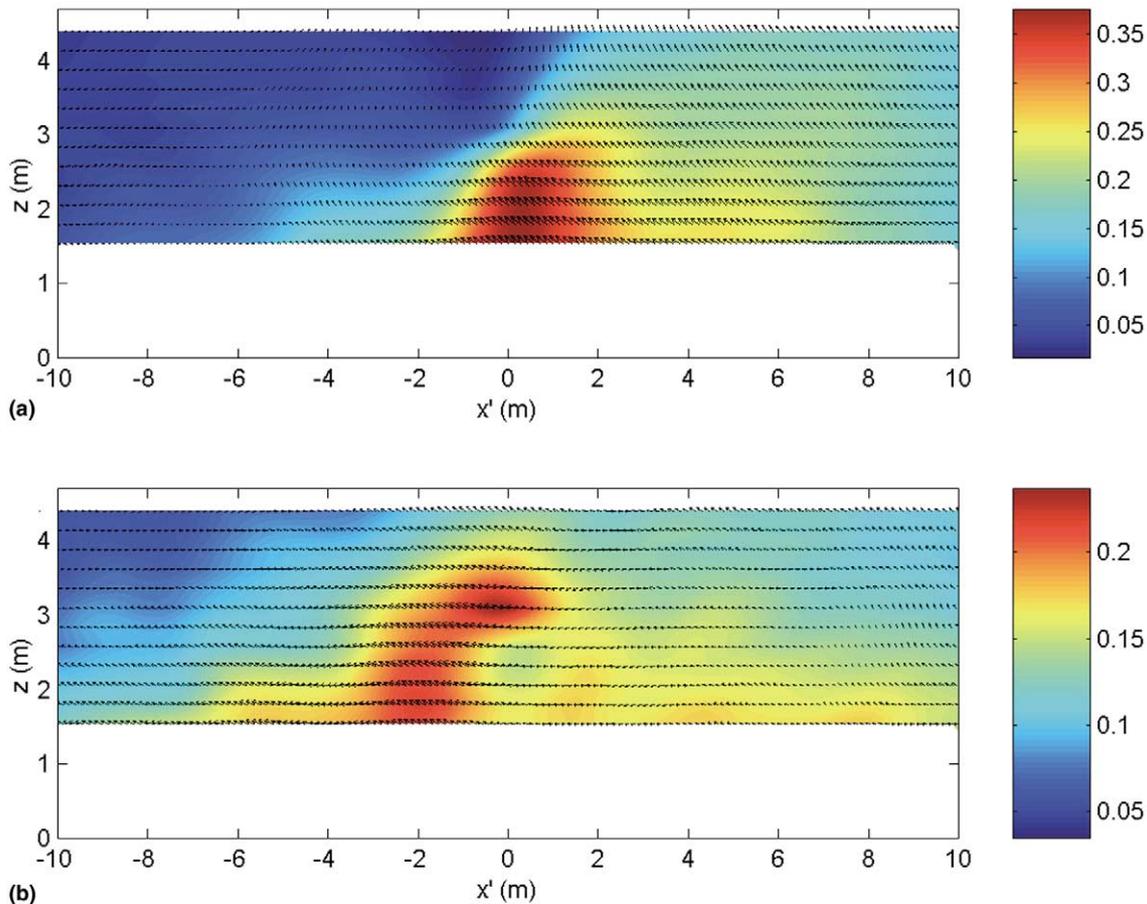


Fig. 14. Conditional averages of the fluctuating part (mean values subtracted) of the resolved velocity field (vectors with streamwise and vertical velocity components) and temperature field (color contour plots – θ' in K), under (a) condition $\beta_{\chi^{2D}(+)}$: $\chi^{2D} > 3 \times \langle \chi^{2D} \rangle$, and (b) condition $\beta_{\chi^{2D}(-)}$: $\chi^{2D} < -\langle \chi^{2D} \rangle$, for measurement period E (unstable).

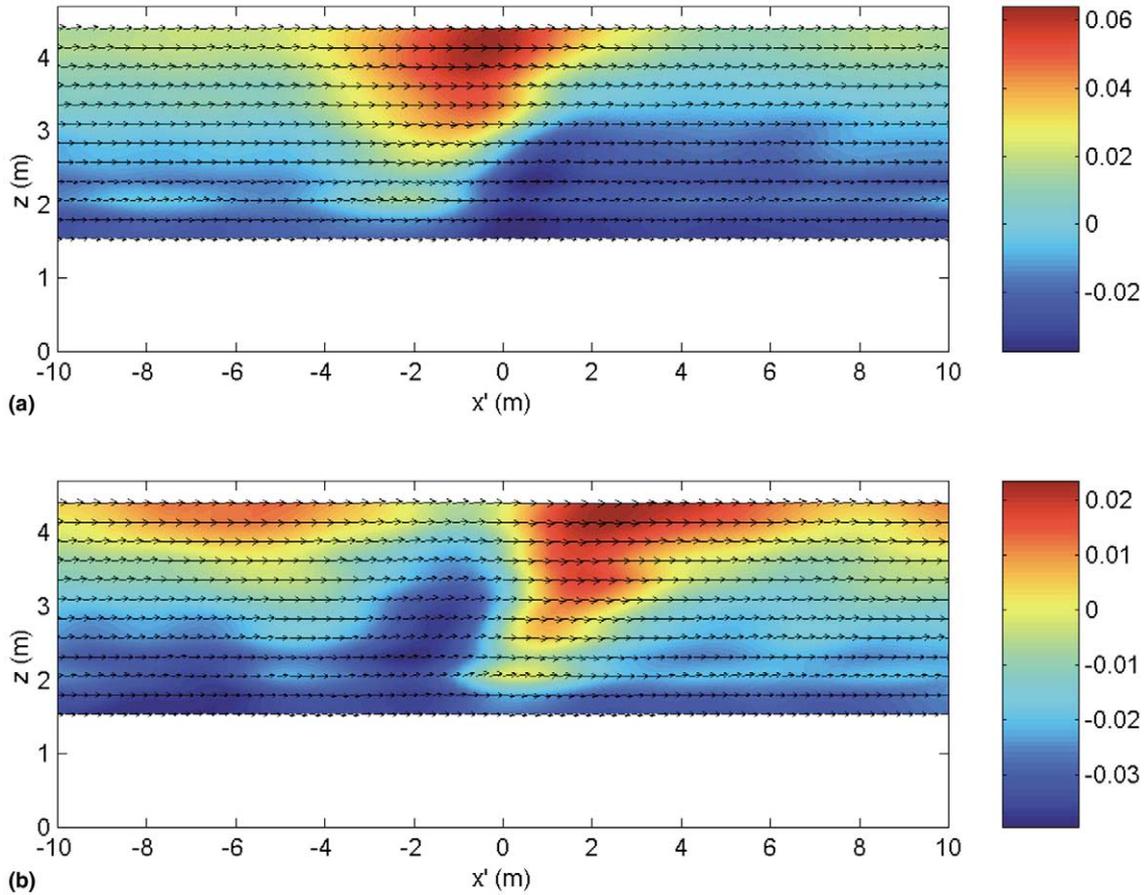


Fig. 15. Conditional averages of the fluctuating part (mean values subtracted) of the resolved velocity field (vectors with streamwise and vertical velocity components) and temperature field (color contour plots $-\bar{\theta}'$ in K), under (a) condition $\beta_{\chi(+)}: \chi^{2D} > 3 \times \langle \chi^{2D} \rangle$, and (b) condition $\beta_{\chi(-)}: \chi^{2D} < -\langle \chi^{2D} \rangle$, for measurement period F (moderately stable).

backscatter is associated with the onset of ejection events at the reference point.

Fig. 15 shows the 2D (streamwise and vertical) conditionally averaged velocity and temperature fields corresponding to the stable period F. An important difference with respect to the unstable case (Fig. 14) is the relatively smaller magnitude of the vertical motions due to the damping effect of stable stratification. Nonetheless, from the conditionally averaged temperature field there is evidence that strong backscatter is associated with the onset of ejection events, the same result as found under unstable conditions (Fig. 15(b)).

4. Conclusions

A field study was carried out in the atmospheric surface layer using 12 3D sonic anemometers to study the effect of atmospheric stability on the SGS heat fluxes and dissipation of the temperature variance. Two distinct arrangements of the sensors are used: First, the instruments were laid out in two horizontal parallel arrays (seven anemometers in the lower array and five in

the upper array). Second, the 12 sensors were arranged vertically.

The first setup, the two horizontal arrays of anemometers, allows us to obtain time series of the SGS fluxes and SGS dissipation at one point in space. These data collected under different atmospheric stability conditions (from unstable to stable stability), were used to study the statistical nature of the SGS variables. The damping of vertical turbulent motions associated with increasing stability has important effects on the statistics of the SGS variables: (a) The relative contribution of the SGS vertical flux $\langle q_3 \rangle$ to the total flux $\langle u'_3 \theta' \rangle$ grows considerably with increasing stability (from 16 % in the moderately unstable case to 47% under very stable conditions). Due to the increased relative importance of the subgrid scales, simulations of stably stratified ABLs are expected to be particularly sensitive to the SGS model formulation. (b) The mean value $\langle \chi \rangle$ of the SGS dissipation of the temperature variance decreased with increasing stability. Negative values, which indicate backscatter (transfer of temperature variance from the subgrid scales to the resolved field) become relatively more important with increasing stability. Hence, LESs

with fully dissipative models, such as the eddy-diffusion model, will inaccurately reproduce the local features of the atmospheric flow under strong stability conditions.

Strong atmospheric stability is associated with a reduction in the characteristic scale of turbulence. For strong enough stability ($L \lesssim \Delta$), the filtering scale Δ falls near (or even outside) the upper limit of the inertial subrange. In that case, inertial subrange arguments (including scale invariance of the SGS model coefficient(s)), on which most SGS models rely, break down. The modeled SGS fluxes and SGS dissipation of the temperature variance, using the eddy-diffusion and non-linear models, are computed to assure that the mean modeled SGS dissipation matches the mean measured SGS dissipation. There is a clear dependence of the model coefficients associated with atmospheric stability. Scale-dependence is particularly strong under strong stability, i.e. when the filter scale approaches and becomes larger than L and the size of eddies is damped by buoyancy effects. This result is in qualitative agreement with existing empirical corrections used to account for stability effects on eddy-viscosity SGS models. However, these empirical models appear to overestimate the effect of stability as compared to our measurements.

The relationship between strong positive/negative SGS dissipation events and coherent structures of the flow (sweeps and ejections) is explored by using two different conditional averaging techniques. First, data from the double horizontal arrays of sensors are used to obtain the conditionally averaged SGS dissipation based on the gradients in the temperature signal. Then, the vertical array of anemometers, the second experimental arrangement, is used to obtain conditionally averaged 2D velocity and temperature fields based on thresholds (large positive and large negative values) in the SGS dissipation during both stable and unstable periods. The results from both conditional averaging methods agree with each other and can be summarized as follows: Under both stable and unstable conditions, strong backscatter is associated with the onset of ejection events while strong forward scatter tends to occur during the onset of sweep events. The relative importance of negative dissipation events becomes larger with increasing stability.

In summary, we have shown that atmospheric stability has important effects on the physics of the subgrid scales, changing their statistical nature (e.g. mean values and pdfs) as well as their relationship to large-scale coherent structures of the flow. However, it is not clear that currently available SGS models have the ability to ‘naturally’ (without any tuning) capture the effect of strong stability on the SGS dynamics. Moreover, for any given SGS model, scale-dependence of the model coefficient(s), associated with a reduction in the characteristic scale of turbulence, poses an additional challenge in simulations of stably stratified ABLs using

dynamic models [17]. New scale-dependent dynamic models, such as the one proposed by Porté-Agel et al. [46], have the potential to yield the correct behavior of the coefficient(s) associated with changes in atmospheric stability.

Acknowledgements

The authors wish to thank their colleagues Pamela Rawe, Elizabeth Jacobs and Joe Arreola from the Johns Hopkins University, William Eichinger, Ahmed Lachab and Zhiming Chen from the University of Iowa, and Roger Shaw and Mike Mata from the University of California at Davis, for fruitful discussions and their invaluable assistance in the field. We also thank Gabriel Katul from Duke University and Jay Ham from Kansas State University for the loan of equipment. Funding from NSF-ATM 9726270 is gratefully acknowledged.

References

- [1] Albertson JD, Parlange MB. Natural integration of scalar fluxes from complex terrain. *Adv Water Res* 1999;23:239–52.
- [2] Albertson JD, Parlange MB. Surface length scales and shear stress: implications for land–atmosphere interaction over complex terrain. *Water Resour Res* 1999;35:2121–32.
- [3] Anderson R, Meneveau C. Effects of the similarity model in finite-difference LES of isotropic turbulence using a Lagrangian dynamic mixed model. *Flow, Turb Combust* 1999;62: 201–25.
- [4] Bardina J, Ferziger JH, Reynolds WC. Improved subgrid scale models for large-eddy simulation. AIAA Paper 1980:80–1357.
- [5] Bastiaans RJM, Rindt CCM, Van AA. Experimental analysis of a confined transitional plume with respect to subgrid-scale modeling. *Int J Heat Mass Transfer* 1998;41:3989–4007.
- [6] Borue V, Orszag S. Local energy flux and subgrid-scale statistics in three-dimensional turbulence. *J Fluid Mech* 1998;366: 1–31.
- [7] Canuto VM, Minotti F. Stratified turbulence in the atmosphere and oceans: a new subgrid model. *J Atmos Sci* 1993;50: 1925–35.
- [8] Canuto VM, Cheng Y. Derivation of the Smagorinsky–Lilly constant C_s . *Phys Fluids* 1997;9:1368–78.
- [9] Cerutti S, Meneveau C. Statistics of filtered velocity in grid and wake turbulence. *Phys Fluids* 2000;12:1143–65.
- [10] Clark RG, Ferziger JH, Reynolds WC. Evaluation of subgrid models using an accurately simulated turbulent flow. *J Fluid Mech* 1979;91:1–16.
- [11] Deardorff JW. Preliminary results from numerical integrations of the unstable planetary boundary layer. *J Atmos Sci* 1970;27:1209–11.
- [12] Deardorff JW. On the magnitude of the subgrid-scale eddy coefficient. *J Comp Phys* 1971;7:120–33.
- [13] Deardorff JW. Stratocumulus-capped mixed layers derived from a three-dimensional model. *Boundary-Layer Meteorol* 1980;18:495–527.
- [14] Domaradski JA, Liu W, Brachet ME. An analysis of subgrid-scale interactions in numerically simulated isotropic turbulence. *Phys Fluids A* 1993;5:1747–59.

- [15] Gao W, Shaw RH, Paw UKT. Observation of organized structure in turbulent flow within and above a forest canopy. *Boundary-Layer Meteorol* 1989;47:349–77.
- [16] Gao W, Shaw RH. Conditional analysis of temperature and humidity microfronts and ejection/sweep motions within and above a deciduous forest. *Boundary-Layer Meteorol* 1992;59:35–57.
- [17] Germano M, Piomelli U, Moin P, Cabot WH. A dynamic subgrid-scale eddy viscosity model. *Phys Fluids* 1991;3:1760–5.
- [18] Gopalakrishnan SG, Roy SB, Avissar R. An evaluation of the scale at which topographical features affect the convective boundary layer using large eddy simulations. *J Atmos Sci* 2000;57:334–51.
- [19] Härtel C, Kleiser L. Energy transfer between large and small scales in wall-bounded turbulent flows. In: Piomelli U, Ragab S, editors. *Engineering applications of large eddy simulations*, vol. 162. New York: ASME, FED; 1993. p. 21.
- [20] Hechtel LM, Moeng C-H, Stull RB. The effects of nonhomogeneous surface fluxes on the convective boundary layer: a case study using large-eddy simulation. *J Atmos Sci* 1990;47:1722–41.
- [21] Hunt JCR, Stretch DD, Britter RE. Length scales in stably stratified turbulent flows and their use in turbulence models. In: Puttock JS, editor. *Stably stratified flows and gas dynamics*. Oxford: Clarendon Press; 1988.
- [22] Katul G, Kuhn G, Schiedge J, Hsieh C-I. The ejection-sweep character of scalar fluxes in the unstable surface layer. *Boundary-Layer Meteorol* 1997;83:1–26.
- [23] Katul G, Hsieh C-I, Sigmon J. Energy-inertial scale interactions for velocity and temperature in the unstable atmospheric surface layer. *Boundary-Layer Meteorol* 1997;82:49–80.
- [24] Kosovic B. Subgrid-scale modelling for the large-eddy simulation of high-Reynolds-number boundary layers. *J Fluid Mech* 1997;336:151–82.
- [25] Krettenauer K, Schumann U. Numerical simulation of turbulent convection over wavy terrain. *J Fluid Mech* 1992;237:261–99.
- [26] Lilly DK. The representation of small-scale turbulence in numerical simulation experiments. In: *Proceedings of the IBM Scientific Computing Symposium on Environmental Sciences*, 1967. p. 195.
- [27] Lin C-L. Near-grid-scale energy transfer and coherent structures in the convective planetary boundary layer. *Phys Fluids* 1999;11:3482–94.
- [28] Lin C-L. Local pressure transport structure in a convective atmospheric boundary layer. *Phys Fluids* 2000;12:1112–28.
- [29] Liu S, Meneveau C, Katz J. On the properties of similarity subgrid-scale models as deduced from measurements in a turbulent jet. *J Fluid Mech* 1994;275:83–119.
- [30] Liu S, Meneveau C, Katz J. Experimental study of similarity subgrid-scale models of turbulence in the far-field of a jet. *Appl Sci Res* 1995;54:177–90.
- [31] Liu S, Katz J, Meneveau C. Evolution and modeling of subgrid scales during rapid straining of turbulence. *J Fluid Mech* 1999;387:281–320.
- [32] Mason PJ. Large-eddy simulation: a critical review of the technique. *Q J R Meteorol Soc* 1994;120:1–26.
- [33] Mason PJ, Derbyshire SH. Large-eddy simulation of the stably-stratified atmospheric boundary layer. *Boundary-Layer Meteorol* 1990;53:117–62.
- [34] Meneveau C. Statistics of turbulence subgrid-scale stresses: necessary conditions and experimental tests. *Phys Fluids* 1994;6:815–33.
- [35] Meneveau C, Katz J. Dynamic testing of subgrid models in LES based on the Germano identity. *Phys Fluids* 1999;11:245–7.
- [36] Meneveau C, Katz J. Conditional subgrid force and dissipation in locally isotropic and rapidly strained turbulence. *Phys Fluids* 1999;11:2317–29.
- [37] Meneveau C, Katz J. Scale-invariance and turbulence models for large-eddy simulation. *Annu Rev Fluid Mech* 2000;32:1–32.
- [38] Meneveau C, O’Neil J. On scaling laws of the dissipation rate of turbulent subgrid-scale energy. *Phys Rev E* 1994;49:2866–74.
- [39] Moeng C-H. A large-eddy simulation model for the study of planetary boundary-layer turbulence. *J Atmos Sci* 1984;46:2311–30.
- [40] Moin P, Squires KD, Lee S. A dynamic subgrid-scale model for compressible turbulence and scalar transport. *Phys Fluids* 1991;3:2746–57.
- [41] O’Neil J, Meneveau C. Subgrid-scale stresses and their modeling in a turbulent plane wake. *J Fluid Mech* 1997;349:253–93.
- [42] Piomelli U, Moin P, Ferziger JH. Model consistency in large eddy simulation of turbulent channel flows. *Phys Fluids* 1988;31:1884–91.
- [43] Piomelli U, Yu Y, Adrian RH. Subgrid-scale energy transfer and near-wall turbulence structure. *Phys Fluids* 1996;8:215–24.
- [44] Pope SB. *Turbulent flows*. Cambridge: Cambridge University Press; 2000.
- [45] Porté-Agel F, Meneveau C, Parlange MB. Some basic properties of the surrogate subgrid-scale heat flux in the atmospheric boundary layer. *Boundary-Layer Meteorol* 1998;88:425–44.
- [46] Porté-Agel F, Meneveau C, Parlange MB. A scale-dependent dynamic model for large-eddy simulation: application to a neutral atmospheric boundary layer. *J Fluid Mech* 2000;415:261–84.
- [47] Porté-Agel F, Parlange MB, Meneveau C, Eichinger WE, Pahlow M. Subgrid-scale dissipation in the atmospheric surface layer: effects of stability and filter dimension. *J Hydrometeorol* 2000;1:75–87.
- [48] Porté-Agel F, Parlange MB, Meneveau C, Eichinger WE. A priori field study of the subgrid-scale heat fluxes and dissipation in the atmospheric surface layer. *J Atmos Sci* 2001;58:2673–98.
- [49] Press WC, Teukolsky SA, Vetterling WT, Flannery BP. *Numerical recipes*. Cambridge: Cambridge University Press; 1992.
- [50] Raupach MR, Antonia RA, Rajagopalan S. Rough-wall turbulent boundary layers. *Appl Mech Rev* 1991;44:1–25.
- [51] Sarghini F, Piomelli U, Balaras E. Scale-similar models for large-eddy simulations. *Phys Fluids* 1999;11:1596–607.
- [52] Schumann U. Subgrid length-scales for large-eddy simulation of stratified turbulence. *Theoret Comput Fluid Dyn* 1991;2:279–90.
- [53] Shaw RH, Tavangar J, Ward D. Structure of the Reynolds stress in a canopy layer. *J Clim Appl Meteorol* 1983;22:1922–31.
- [54] Shaw RH, Paw UKT, Gao W. Detection of temperature ramps and flow structures at a deciduous forest site. *Agric Meteorol* 1989;47:123–38.
- [55] Shaw RH, Schumann U. Large-eddy simulation of turbulent flow above and within a forest. *Boundary-Layer Meteorol* 1992;61:47–64.
- [56] Smagorinsky J. General circulation experiments with the primitive equations, Part 1: the basic experiment. *Mon Weather Rev* 1963;91:99–164.
- [57] Sullivan PP, McWilliams JC, Moeng C-H. A subgrid-scale model for large-eddy simulation of planetary boundary-layer flows. *Boundary-Layer Meteorol* 1994;71:247–76.
- [58] Szilagyi J, Parlange MB, Katul GG, Albertson JD. An objective technique for determining principal time scales of coherent eddy structures using orthogonal wavelets. *Adv Water Res* 1999;22:561–6.

- [59] Tong C, Wyngaard JC, Khanna S, Brasseur JG. Resolvable- and subgrid-scale measurement in the atmospheric surface layer: technique and issues. *J Atmos Sci* 1998;55:3114–26.
- [60] Tong C, Wyngaard JC, Brasseur JG. Experimental study of the subgrid-scale stresses in the atmospheric surface layer. *J Atmos Sci* 1999;56:2277–92.
- [61] Vreman B, Geurts B, Kuerten H. Large eddy simulation of the turbulent mixing layer. *J Fluid Mech* 1997;339: 357–90.